

[Work in progress] Scalable, out-of-the box segmentation of individual particles from mineral samples acquired with micro CT

Karol Gotkowski^{a,b}, Shuvam Gupta^c, Jose R. A. Godinho^c, Camila G. S. Tochtrop^c, Klaus H. Maier-Hein^{b,d} and Fabian Isensee^{a,b,*}

^aHelmholtz Imaging, German Cancer Research Center, Im Neuenheimer Feld 280, Heidelberg, 69120, Baden-Wuerttemberg, Germany

^bDivision of Medical Image Computing, German Cancer Research Center, Im Neuenheimer Feld 280, Heidelberg, 69120, Baden-Wuerttemberg, Germany

^cHelmholtz-Zentrum Dresden-Rossendorf, Helmholtz Institute Freiberg for Resource Technology, Chemnitzer Straße 40, Freiberg, 09599, Sachsen, Germany

^dPattern Analysis and Learning Group, Department of Radiation Oncology, Heidelberg University Hospital, Im Neuenheimer Feld 672, Heidelberg, 69120, Baden-Wuerttemberg, Germany

ARTICLE INFO

Keywords:

individual particle characterization
3D
instance segmentation
deep learning

ABSTRACT

Minerals are indispensable for a functioning modern society. Yet, their supply is limited causing a need for optimizing their exploration and extraction both from ores and recyclable materials. Typically, these processes must be meticulously adapted to the precise properties of the processed particles, requiring an extensive characterization of their shapes, appearances as well as the overall material composition. Current approaches perform this analysis based on bulk segmentation and characterization of particles, and rely on rudimentary postprocessing techniques to separate touching particles. However, due to their inability to reliably perform this separation as well as the need to retrain or reconfigure most methods for each new image, these approaches leave untapped potential to be leveraged. Here, we propose an instance segmentation method that is able to extract individual particles from large micro CT images taken from mineral samples embedded in an epoxy matrix. Our approach is based on the powerful nnU-Net framework, introduces a particle size normalization, makes use of a *border-core* representation to enable instance segmentation and is trained with a large dataset containing particles of numerous different materials and minerals. We demonstrate that our approach can be applied out-of-the box to a large variety of particle types, including materials and appearances that have not been part of the training set. Thus, no further manual annotations and retraining are required when applying the method to new mineral samples, enabling substantially higher scalability of experiments than existing methods. Our code and dataset are made publicly available.

1. Introduction

Mineral resources are ubiquitous in modern society, yet, they constitute a finite resource that needs to be acquired cost-effectively and used responsibly. Our ability to extract raw materials from the earth's crust is remarkable, and so are the recent advances in mineral exploration, ore processing, reservoir characterization, and the developed technologies to reuse materials through recycling. Moreover, with the ever-rising demand for mineral resources [1], these processes are becoming increasingly automated. Characterization of mineral particles plays a crucial role in this process by providing a detailed understanding of the minerals and enabling the development of effective automated processes.

So far, bulk characterization of mineral particles embedded in an epoxy matrix and imaged via computed tomography (CT) is the most frequently used method for optimizing these processes. Realized through semantic segmentation that segments all particles without distinguishing between particle instances, it is either performed through a variation of intensity thresholding Hassan, Airey, Khan and Collop

(2012); Becker, Jardine, Miller and Harris (2016); Dominy, Platten, Howard, Elangovan, Armstrong, Minnitt and Abel (2011); Godinho, Kern, Renno and Gutzmer (2019) or deep learning approaches Wang, Li, Xiao, Zhang, Miao and Wang (2021); Filippo, Gomes, da Costa and Mota (2021); Xiao, Liu, Le, Ji and Sun (2020); Latif, Bouchard, Maitre, Back and Bédard (2022); Nie, Zhang and Cao (2022); Liu, Zhang, Liu, Wang and Xia (2021); Tung, Halim, Wang, Rich, Marjo and Regenauer-Lieb (2022). The individual particle properties that determine the behavior of each particle are not accounted for in this type of analysis, limiting our understanding of the used minerals and our ability to optimize downstream processes.

A better optimization can be achieved with the characteristics of individual particles Pereira, Frenzel, Khodadadzadeh, Tolosana-Delgado and Gutzmer (2021), referred to as instance segmentation, in which every particle instance is segmented and assigned a unique identifier. This has the advantage that each particle can be further characterized individually according to its specific shape, size, and particle histogram[XXX]. Such attempts to characterize individual particles have been mostly limited to imaging techniques that analyze only a single 2D image Liu, Zhang, Jing, Wang and Zhao (2020); Baraian, Kellokumpu, Paaso, Koresaar and Kaartinen (2022); Sun, Huang, Cheng, Jia, Xiong and Zhang (2022), leading to an inherent stereological bias that makes

*Corresponding author

✉ karol.gotkowski@dkfz.de (K. Gotkowski); s.gupta@hzdr.de (S. Gupta); j.godinho@hzdr.de (J.R.A. Godinho); guimar75@hzdr.de (C.G.S. Tochtrop); klaus.maier-hein@dkfz-heidelberg.de (K.H. Maier-Hein); f.isensee@dkfz-heidelberg.de (F. Isensee)

ORCID(s):

the shape and size quantification of particles unreliable Blannin, Frenzel, Tuşa, Birtel, Ivăşcanu, Baker and Gutzmer (2021).

Extending individual particle characterization to 3D is challenging, given that upwards of ten thousand particles are typically present in a single image. Even more, the presence of imaging artifacts as well as highly diverse appearances of particles and filler materials make this a difficult problem where established methods that rely on intensity thresholding Zhou, Dai, Cheng, Thompson and Leach (2021); Jiang, Shen, Guillard and Einav (2021); Wang, Lin and Miller (2016, 2015); Guntoro, Ghorbani, Parian, Butcher, Kuva and Rosenkranz (2021); Godinho, Grilo, Hellmuth and Siddique (2021) may fail due to their lack of robustness. To solve this problem for 3D instance segmentation more sophisticated deep learning methods are a necessity Furat, Kirstein, Leißner, Bachmann, Gutzmer, Peuker and Schmidt (2023); Tang, Da Wang, Niu, Honeyands, O'Dea, Mostaghimi, Armstrong and Knackstedt (2023) as they use a multitude of learned features, making them inherently more robust to these challenges. However, a limitation of these approaches is constituted through the use of semantic segmentation models to generate predictions that are converted in a separate postprocessing step into instance segmentations, leading to touching particles often not recognized as separate instances and thus falsifying any further analysis. Moreover, a common drawback of all current deep learning approaches used for particle segmentation is the narrow scope on specific types of minerals, resulting in a lack of generalization. Consequently, these methods do not work out-of-the-box when applied to a new particle dispersion image as part of the image needs to be annotated manually and the methods retrained in order to function properly.

To truly pave the way for process optimization based on individual 3D particle characterization, we propose an automated out-of-the-box 3D instance segmentation method with high robustness and generalizability that can handle diverse sample and particle types across magnitudes of different particle sizes without the need to adapt the method or annotate new data and thus does not constitute major bottlenecks. Our approach employs a highly optimized novel training and inference pipeline based on a 3D U-Net and is trained on a large dataset of particle dispersion CT images with a multitude of different materials and minerals. Thus our approach enables a wide range of analyses based on the intrinsic particle properties measurable based on the inferred instance segmentations and can be employed even by non-machine learning experts without prior knowledge. Our framework and all data are open source and available under XXX

2. Materials

2.1. Sample preparation

The samples used in our approach consist of dispersed particles prepared using a standardized procedure (Godinho et al. 2021a) that uses sugar particles as spacers in the ratio of 7 g of sugar to 1 g of sample particles. The resin used

is Paladur (Kulzer, Mitsui Chemical Group), a fast-curing acrylic polymer. The particles of the material together with the sugar were mixed with methylmethacrylate-copolymer powder in a mass ratio of 1:1. The methylmethacrylate liquid resin was added to the solid mixture in a ratio of 3 mL to 10 g. The final paste is left to dry in a tube with a diameter adequate for the desired voxel size of the scan. Samples were imaged with a CT scanner (CoreTom from XRE – Tescan; Ghent, Belgium), while the “XRE – recon” software (v1.1.0.14, XRE – Tescan, Ghent, Belgium) was used to reconstruct the 3D images. Scanning conditions differed on a per-sample basis as to use optimal reconstruction parameters based on material and mineral compositions. Consequently, voxel intensities and particle sizes vary between the obtained images. Reconstructed images were processed as 16-bit images and visualizations were performed using Avizo software (v9.3.0, Thermo Fisher Scientific, Waltham, MA, USA) and Dragonfly software (v2021.1, Objects Research Systems, Montreal, Quebec, Canada).

2.2. Datasets

A diverse set of samples is required in order to train a model that predicts high-quality instance segmentations and generalizes well even to materials and minerals not present in the training distribution. The samples prepared for our approach cover a wide range of materials, e.g. natural ores, slags, and recyclable materials like batteries and crushed electronic devices to fulfill this criterion. For the development and training of our method, 19 samples were prepared in total from which we used 41 patches with either a size of 128x400x400 or 200x400x400 voxels that had been extracted and annotated following the procedure outlined in section 3.1. An example of such a prepared and annotated sample is shown in Figure 1. Model optimization was performed by running stratified 5-fold cross-validation on these patches and quantitatively evaluating the result. For testing the performance of our model, we designed two test sets reflecting different use cases. The first is an in-distribution set of in total 8 patches from 8 samples, with the purpose to evaluate the performance in terms of its prediction quality on samples that consist of materials and minerals already seen by the framework during training. The second is an out-of-distribution set with in total 5 patches from 5 samples, consisting of materials and minerals entirely or in their composition unknown to the model to evaluate the generalization abilities of our method. A listing of all samples is given in Table 1. The datasets are available online at...

3. Methodology

Instance segmentation of 3D voxel images is still a problem mostly solved with classical methods. 3D instance segmentation models based on deep learning exist [XXX] but have not been extensively used and evaluated for generalization and robustness in practice. On the contrary, 3D semantic segmentation is a well-studied task with a variety of suitable models proven successful such as U-Nets

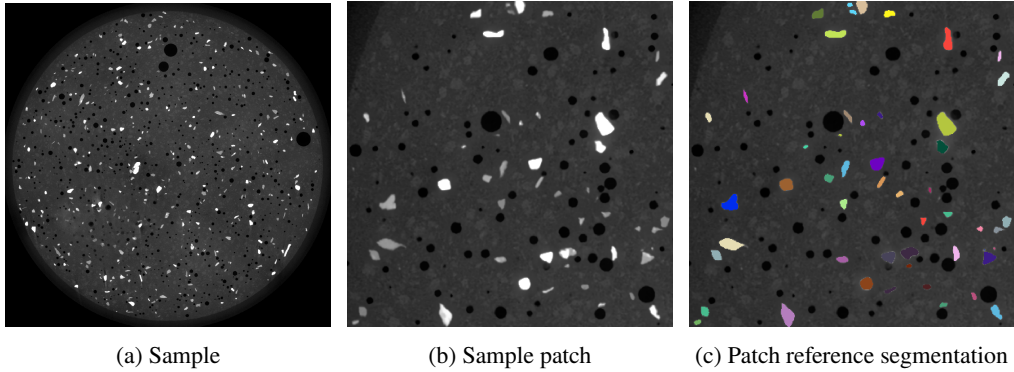


Figure 1: Overview of the image Ore1_Zone3_Concentrate and its reference segmentation.

Sample	Mineralogy	Physical Particle Size (μm)	Set
Ore1_Zone1_Feed	XXX	XXX	
Ore1_Zone2_Concentrate	XXX	XXX	
Ore1_Zone3_tailings	XXX	XXX	
Recycling1	XXX	XXX	
Ore2_PS300_VS10	XXX	XXX	
Ore2_PS850_VS26	XXX	XXX	
Ore2_PS75_VS5p5	XXX	XXX	
Synthetic1	XXX	XXX	
Slag3_PS200	XXX	XXX	
Tmp6	XXX	XXX	
Ore3_Zone3	XXX	XXX	
Ore8	XXX	XXX	
Slag6_PS500	XXX	XXX	
Synthetic3	XXX	XXX	
Synthetic_Tmp8	XXX	XXX	
Synthetic_Tmp9	XXX	XXX	
Synthetic_Tmp10	XXX	XXX	
Synthetic_Tmp11	XXX	XXX	
Synthetic_Tmp12	XXX	XXX	
Ore1_Zone3_Concentrate	XXX	XXX	
Slag5_3	XXX	XXX	
TmpName_001	XXX	XXX	
Ore2_PS850_VS10	XXX	XXX	
Slag6_PS300	XXX	XXX	
Ore3_Zone1	XXX	XXX	
Ore3_Zone2	XXX	XXX	
Slag3_PS300	XXX	XXX	
Slag4_1	XXX	XXX	
Ore5	XXX	XXX	
Ore4_PS_Tmp3	XXX	XXX	
Ore4_PS_Tmp4	XXX	XXX	
Ore7	XXX	XXX	

Table 1

A listing of all particle dispersion samples, their mineralogical composition, and physical particle size range that have been used for the train set, in-distribution (ID) test set, and out-of-distribution (OOD) set.

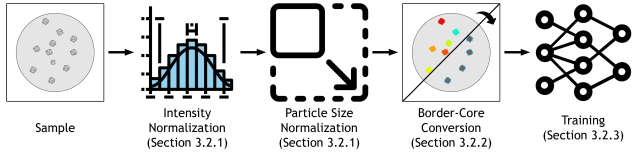
and Transformers. Especially nnU-net, a state-of-the-art 3D semantic segmentation model, has proven its performance, generalization abilities, and robustness on a number of challenges it has won XXX. However, converting the semantic segmentations predicted by such models into instance segmentations is challenging as particles tend to have inconsistent shapes and are often intertwined with each other. In order to handle such cases, we reformulate the instance segmentation problem as a semantic segmentation problem by converting the instances to a border-core representation,

elaborated in 3.2.2, enabling the usage of nnU-Net for 3D instance segmentation. With this technique at its core, we propose a new deep learning based method as depicted in 2 that enables a fully automated generation of instance segmentations for individual particle characterization in 3D CT images. The optimized annotation pipeline developed for this task and proposed in section 3.1 is used to create training data for our method due to a lack of openly available reference instance segmentation data. Subsequently, we use the data in our training pipeline, as described in section 3.2, to train a robust model that generalizes well even to unseen types and compositions of materials and minerals. As a result, no additional training data or finetuning is required for the inference process described in section 3.3.

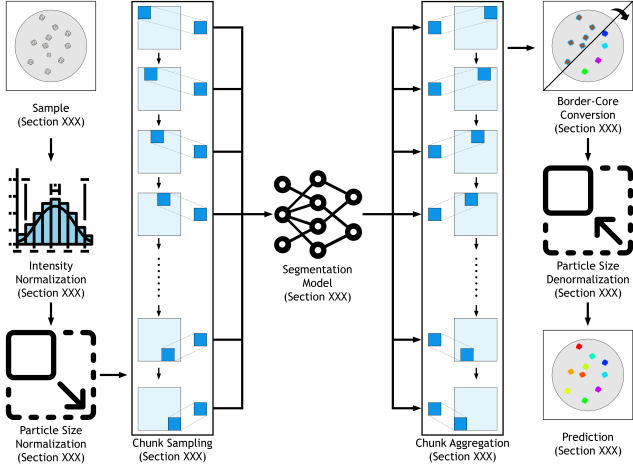
3.1. Reference annotation

3D images of particle dispersions typically contain thousands of individual particles. Annotating entire images, even with the support of our proposed annotation pipeline, is too labor-intensive and would yield mostly redundant information for our method. Thus, utilizing the heterogeneity of the images, we take one or several representative smaller patches from each training sample for annotation. To enable fast and precise annotations the interactive 3D viewer Napari Sofroniew, Lambert, Evans, Nunez-Iglesias, Bokota, Winston, Peña-Castellanos, Yamauchi, Bussonnier, Pop et al. (2022) is used with multiple plugins to guide the annotation process. A guide for the annotation process is available at... For each patch, a semantic segmentation of the particles is performed through the use of a Random Forest voxel classifier that is trained with scribble annotations. Random Forest classifiers operate on a broad set of handcrafted image features such as intensity gradients, image intensities, and gradient orientations making them more robust against CT imaging artifacts. The segmentation process is iteratively repeated with more refined scribbles until the result is satisfactory. Once completed, remaining errors are corrected fully manually. An example of this random forest segmentation is shown in Figure 3.

The semantic segmentation is then converted into an instance segmentation by assigning all particles a unique identifier. Particles touching each other are incorrectly given



(a) The training pipeline of our method. Intensities and particle sizes of the train patches are normalized with a subsequent conversion of the instance segmentations into the border-core representation. The image patches and segmentations are subsequently used for the training of the nnU-Net model.



(b) The inference pipeline of our method. Intensities and particle sizes of the image are normalized and chunked patches sampled with the chunk sampler. A border-core representation is predicted by the nnU-Net for all patches which are subsequently aggregated into an image prediction that is converted into an instance segmentation and at last denormalized back to original image size.

Figure 2: The training and inference pipelines of our method.

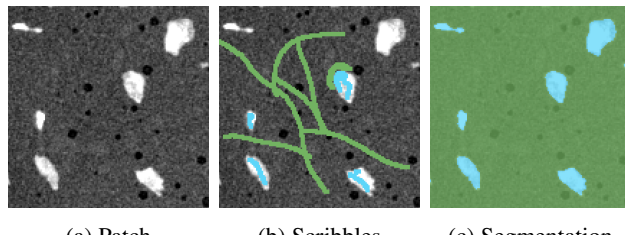
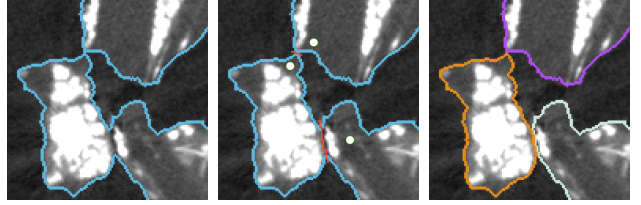


Figure 3: Annotation process of creating a semantic segmentation with Random Forest through iterative refinement with scribbles. (a) A patch is extracted from the image; (b) Scribbles are iteratively refined in the patch; (c) A semantic segmentation of the particles is successfully created.

only a single identifier in this step, which must subsequently be corrected. For this, a custom particle-splitting tool developed by us is utilized. A marker is placed on each particle and a border is drawn between the particles. The particle-splitting tool then computes the geodesic distance[XXX] of each voxel in both particles to the defined 2D border and separates them by applying a watershed algorithm on the geodesic distances with the particle markers as seeds for the



(a) Touching Particles (b) Splitting Process (c) Split Particles

Figure 4: Annotation process of separating touching particles in order to create an instance segmentation. (a) Touching particles are identified; (b) A marker is placed on each particle and a 2D border is defined with our particle splitting tool; (c) The particles are successfully separated in 3D and each is assigned a unique identifier.

algorithm. The result is a well-defined 3D border between the two particles in most cases requiring only a few seconds of annotation time. The process of this particle separation is depicted in Figure 4.

3.2. Training pipeline

The training pipeline, depicted in Figure 2a, consists first of a preprocessing stage to normalize the pixel intensities and homogenize the particle sizes to cope with the size changes of multiple orders of magnitude (Section 3.2.1). Next, a border-core representation, shown to perform well for large-scale cell tracking Isensee, Jaeger, Kohl, Petersen and Maier-Hein (2021) and thus suitable for identifying particles in the ten thousands, is used to map the reference instance segmentations to semantic segmentations (Section 3.2.2). The border-core representations are then used for training nnU-Net, which has been proven highly successful on a multitude of diverse datasets (Section 3.2.3).

3.2.1. Preprocessing

Voxel intensities I of all images are normalized via z-scoring. To this end, the global mean intensity μ and standard deviation of intensities σ are computed over all training images. Then, each voxel intensity is normalized I_{norm} with the following Equation 1.

$$I_{norm} = \frac{I - \sigma}{\mu} \quad (1)$$

Particle sizes typically vary substantially, from XXX to YYY micrometers. At the same time, CT images are acquired at varying voxel sizes. Consequently, the size of particles in voxels varies substantially between images. We hypothesize that such a broad size distribution hampers the training of the segmentation model, causing reduced performance and reduced robustness. To counteract this problem, we strive to homogenize the particle size distribution in our training data. To this end, the original particle size of a sample is determined by measuring the diameter of a particle that is about average size within the sample. No sophisticated methods are required for this as the particle size only needs

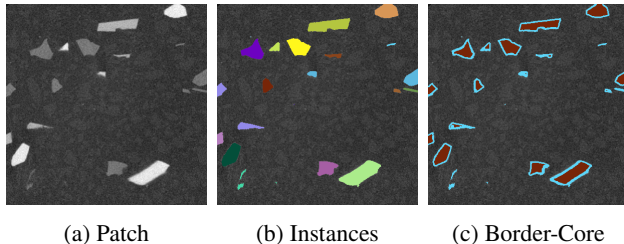


Figure 5: The conversion process of a patch (a) from its instance segmentation (b) into its corresponding border-core representation (c).

to be roughly correct. All training patches are then resized to a common average patch size.

3.2.2. Border-core representation

A border-core representation enables any semantic segmentation model to be used for instance segmentation. In contrast to ad-hoc conversion methods such as watershed which often fail to correctly separate instances, a border-core representation is more advantageous due to the intrinsic properties of the representation which are subsequently learned by the model during training. An example of this representation is shown in Figure 5. Conversion to the border-core representation is achieved by eroding every instance with a fixed width in voxels (see section 4.2) referred to as border thickness to generate a core, while the eroded area represents the border of a particle. As a result, the intrinsic properties of this representation are that every particle has the same border thickness and that no core of an instance is connected to a core of another instance. Training a model with such a representation enables the model to learn these properties and replicate them during inference. Such predicted border-core representation can then be easily converted back into instance segmentations by assigning each core a unique identifier and dilating the cores back to the original particle shape as defined by the border.

3.2.3. Model training

We use nnU-Net Isensee et al. (2021) as the semantic segmentation model in our training and inference pipeline. nnU-Net is a self-adapting 3D U-Net that creates a finger-print of relevant properties from a dataset and automatically adapts important training hyperparameters accordingly. Originally developed for 3D biomedical data and becoming a state-of-the-art model on multiple medical benchmark datasets XXX, nnU-Net has also shown its efficacy in other domains such as XXX, XXX, and XXX. Its consistent performance across multiple domains makes it an ideal fit for the task of mineral particle segmentation in high-resolution CT images. No modifications have been made to nnU-Net, except for a touching particle augmentation, which is detailed in the following.

To a large degree nnU-Net is able to learn on its own the intrinsic properties of a border-core representation based on the already existing touching particles in the training data.

However, the number of touching particles in the training data used in our method is too small for nnU-Net to fully prevent the miss-prediction of touching particles during inference. This leads to some touching particles being merged into a single particle. To reduce this error and to further improve the nnU-Net training, we introduce a touching particle augmentation. This augmentation is applied on every image patch in a batch during a training iteration with a certain probability. It selects a random particle within the current patch (particle P) and a random particle taken from the entire training dataset (particle D) and copies particle D next to particle P such that their particle edges touch each other. This way, nnU-Net learns over time a better understanding of how to correctly identify touching particles as separate instances and consequently predict a better border-core representation.

3.3. Inference pipeline

Inference on a new image is performed by first normalizing its voxel intensities (Section 3.2.1). The actual inference is done in a chunk-patch-based sliding window approach as the entire sample is too large to store in GPU memory (Section 3.3.1). For each patch, the particle size normalization (Section 3.2.1) is performed on-the-fly and the patch is subsequently passed to the model for predicting the border-core segmentation (Section 3.2.2). Once a patch is predicted, its local patch prediction is inserted into its original position in the global prediction of the sample, aggregating all patches during the inference process into a final prediction. This prediction is at last converted into an instance segmentation and resampled back to its original particle size, concluding the inference process. A depiction of the inference pipeline is shown Figure 2b.

3.3.1. Chunk sampling and aggregation

A sliding window approach with a patch sampler as depicted in Figure 6a is used during inference as the entire sample is too large to store in GPU memory. In order to still achieve the best possible quality, it has proven successful to use a patch overlap when using a sliding window approach. This means that except for the image edges, every voxel in the sample is predicted multiple times by the model, and the resulting predictions for a voxel are averaged. The model predicts class probabilities for every voxel in a patch and after the sliding window has reached the end of the sample, the predicted class probabilities of the sample are converted into the border-core segmentation. However, this approach reaches technical limitations for large images as in our case as the averaged patch predictions of every patch depend on all surrounding patches. Consequently, all predicted patches are required to be stored in memory, resulting in infeasibly large memory consumption of often more than 100 GB. To solve this issue, we developed a chunk-patch sampling strategy as depicted in Figure 6b. The sample is subdivided into multiple chunks. Each chunk has an overlap with the neighboring chunks of exactly one patch, ensuring that voxels at the edges of a chunk are also predicted multiple times through the patch overlap such that the prediction quality

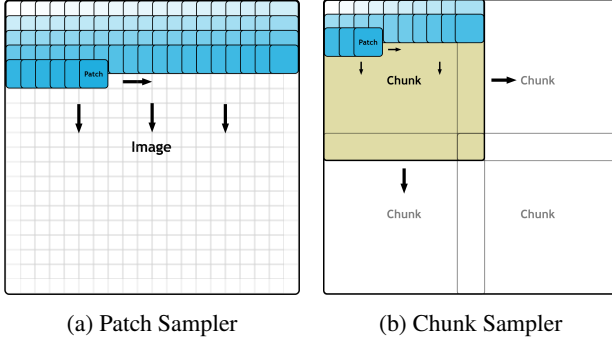


Figure 6: Sampling process of a patch sampler compared to our developed chunk sampler that overcomes the limitations of the patch sampler.

does not decrease at the chunk edges. A prediction is inferred for each chunk with the sliding window approach and subsequently saved to disk. This enables a memory-efficient inference of large images as only a single chunk is kept in memory at all times without compromising segmentation quality and adds only a minimal inference time overhead.

4. Experimental Setup

4.1. Evaluation metrics

The quality of the inferred instance segmentations is quantitatively measured with multiple metrics and can be divided into the categories of segmentation quality metrics (Section 4.1.1) and separation quality metrics (Section 4.1.2) which are introduced in the following sections.

4.1.1. Segmentation quality metrics

We use in total three metrics to measure the quality of the inferred predictions. The $F1$ score (Equation 2), also known as *Dice* score, is the most commonly used metric in image segmentation tasks to measure the ability of a method to correctly assign pixels to either foreground or background. However, it does not consider different particles and thus does not measure whether pixels are assigned to the correct particle. The $F1_{match}$ score (Equation 3) measures how well particles were recognized, regardless of how accurately they are delineated. The $F1_{instance}$ score (Equation 4) considers both segmentation quality as well as the correct identification of particles and is thus the metric most indicative of the performance of our method.

The ranges of all three metrics are within $[0, 1]$ with a higher score indicating a better segmentation quality. All metrics are based on a confusion matrix CM with true positives, false positives, true negatives, and false negatives being denoted as TP , FP , TN , and FN , respectively. Further, the confusion matrix CM is computed in three different variations:

- Let CM_v be the confusion matrix that is computed over all voxels v in a prediction and its respective reference.

- Let CM_m be the confusion matrix that is computed over the count of all matched and mismatched particles m with a match being defined as two particles having a minimum 0.1 $F1$ overlap of its particle voxels.
- Let CM_i be the confusion matrix that is computed over the voxels i of a single particle instance in a prediction and its respective reference with I denoting all particles instances.

$$F1 = \frac{2TP_v}{2TP_v + FP_v + FN_v} \quad (2)$$

$$F1_{match} = \frac{2TP_m}{2TP_m + FP_{ms} + FN_m} \quad (3)$$

$$F1_{instance} = \frac{\sum_i^I \frac{2TP_i}{2TP_i + FP_i + FN_i}}{\sum_i^I 1} \quad (4)$$

4.1.2. Separation quality metrics

An issue that can arise when inferring an instance segmentation is the incorrect identification of touching particles into a *Merger* particle. Similarly, a single particle can incorrectly be split into multiple particles resulting in a *Splitter*. It is highly relevant to reduce the number of such *Mergers* and *Splitters* as they falsify any later downstream analysis. To evaluate the robustness of our method against such misidentification, we introduce the *MergerRatio* and *SplitterRatio* to quantify these errors and define them in the following.

Let P be the set of all particles and let M be a set of each other touching particles that is misidentified and merged into a single particle. Further, let GM be a set of all touching particle sets M that are incorrectly predicted. The *MergerRatio* is then defined as in Equation 5. It is important to highlight that M and GM are defined on the predicted segmentation while P is defined on the reference segmentation in order to enable a comparison between methods as different methods predict different numbers of particles.

$$MergerRatio = \frac{(\sum_{M_i}^{GM} |M_i|) - |GM|}{|P|} \quad (5)$$

The *SplitterRatio* can be defined similarly.

Let P be the set of all particles and let S be a set of incorrectly predicted split particles all part of the same reference particle. Further, let GS be a set of all splitter sets S . The *SplitterRatio* is then defined as in Equation 6. Again, it is important to highlight that S and GS are defined on the predicted segmentation while P is defined on the reference segmentation. The ratios for both the *MergerRatio* and the *SplitterRatio* can theoretically be in the range $[0, \infty)$ but are

in practice smaller than 1 with a lower ratio indicating a lower number of *Mergers* and *Splitters*.

$$\text{SplitterRatio} = \frac{(\sum_{S_i}^{GS} |S_i|) - |GS|}{|P|} \quad (6)$$

4.2. Training configuration

The training of the nnU-Net is done in PyTorch with SGD optimizer, a learning rate of 1e-2, a weight decay of 3e-5, a momentum of 0.99, and 1000 epochs of training time. A target particle size of 60 voxels is used in the particle normalization stage. In the border-core to instance conversion stage, the small core removal filter uses a minimum distance of 1 with a threshold of 0.95, and in the final postprocessing stage, the small particle filter uses a relative minimum particle size of 0.005.

4.3. Comparison with traditional particle segmentation

We intend to compare our method against other frequently used methods quantitatively and qualitatively in section 5. Consequently, we reviewed common segmentation and postprocessing strategies used to create instance segmentations in order to derive the standardized instance segmentation method ThreshWater, which is described in the following section 4.3.1.

4.3.1. ThreshWater

Individual particle characterization via instance segmentation is mostly performed through thresholding followed by a postprocessing step designed to label individual particles and separate the ones that are touching each other. We facilitate the same method and use it for comparison to our method. Considering that intensity values differ greatly between samples, the threshold is manually tuned for each image. To combat poor performance in low-contrast images, we erode the resulting noisy particle mask to suppress an overwhelming number of small false positive particle detections while retaining the integrity of the true positive larger particles. To convert this semantic segmentation into an instance segmentation where the particles are separated and can be processed individually, we again follow best practices and make use of a watershed-based Van der Walt, Schönberger, Nunez-Iglesias, Boulogne, Warner, Yager, Gouillart and Yu (2014) splitting procedure. Seed points are generated by eroding the particle mask. The seeds together with the masks are then used by the watershed algorithm [cite the implementation you used] to separate the particles. Both the amount of erosion for the noise reduction and the amount of erosion for the core generation have been optimized on the train dataset.

5. Results

Evaluation of our approach has been conducted quantitatively (section 5.1), qualitatively (section 5.2), and with respect to inference time (section 5.3) on an in-distribution

and out-of-distribution test set which are elaborated in more detail in section 5.1. Reference segmentations for both test sets have been created as described in section 3.1 and have been used to evaluate our predictions. Further, we also evaluated the method ThreshWater (section 4.3.1) in the same fashion as our method and used it as a baseline. Training of our method was exclusively carried out on the 41 train set patches as detailed in section 2.2.

5.1. Quantitative evaluation

Quantitative method performance is measured using the $F1$ score, the $F1_{match}$ score, and the $F1_{instance}$ score. In addition, we perform an in-depth analysis of the method's ability to correctly split touching particles using the *Merger Ratio* and the *SplitterRatio*. For a complete description of the metrics used, see section 4.1.

5.1.1. In-Distribution evaluation

The in-distribution test set consists of samples with materials and minerals similar to the ones used during training and evaluation of such samples provides an estimate of the model's performance on types of samples the model will encounter in real-world use cases. In total, the set contains 8 manually annotated patches from 8 samples as described in section 2.2. We quantitatively evaluate the predictions of our proposed method as well as those of ThreshWater using the metrics introduced in section 4.1. The $F1$, the $F1_{match}$, and $F1_{instance}$ results for our method and ThreshWater are shown in Figure 7 and in Table 2. On average, a $F1$ of 94.84% is achieved over all samples. Even on the individual samples, the $F1$ is above 93%, indicating a high segmentation quality for every sample. Our average $F1$ is 1.01% better than that of ThreshWater, which is a substantial improvement at this level of precision. This is especially notable given the fact that ThreshWater uses a manually tuned threshold for each sample whereas our method is applied out-of-the-box. For the $F1_{match}$ score we achieve a score of 95.16% on average over all samples, implying a high correct identification rate of individual particles as instances, which is amongst the most important properties of an instance segmentation. By comparison, ThreshWater only achieves an $F1_{match}$ score of 82.58%, which is 12.58% less than that of our method and indicates only a moderate identification rate of individual particles. In terms of the $F1_{instance}$ metric, our method achieves a score of 82.13% on average while ThreshWater only achieves a score of 69.29% and is thus 12.84% worse compared to our method. It thus shows that ThreshWater performs poorly in comparison to our method in terms of individual particle segmentation and particle identification as measured by the $F1_{instance}$ metric.

Following up on the segmentation quality evaluation, we continue with the discussion on the separation quality evaluation with the *Merger Ratio* and the *SplitterRatio*. The results of our method and ThreshWater are depicted in Figure 8 and Table 3. The reference patches from the test samples contain a total of 3020 particles. Of those 3020 particles only 198 particles are touching, which amounts to 7% of the particles. This can be attributed to our sample preparation

Name	$F1$	$F1_{match}$	$F1_{instance}$
ThreshWater	0.9383	0.8258	0.6929
Ours	0.9484	0.9516	0.8213

Table 2

The segmentation quantification results of the in-distribution set of our method compared to ThreshWater. Higher is better.

technique, in which a spacer is used to separate individual particles as much as possible from each other. Of those 198 touching particles, only 64 Mergers have been falsely created by our method and 88 Mergers by ThreshWater, which results in a *Merger Ratio* of 1.31% and 2.67%, respectively. In terms of Splitters, only 11 Splitters in total are created by our method in comparison to 329 Splitters created by ThreshWater, which results in a *Splitter Ratio* of 0.58% and 9.02%, respectively. This shows that Splitters are mostly not a problem with our approach, while ThreshWater is prone to create a high number of Splitters, for which the reasons are explored in section 5.2.4.

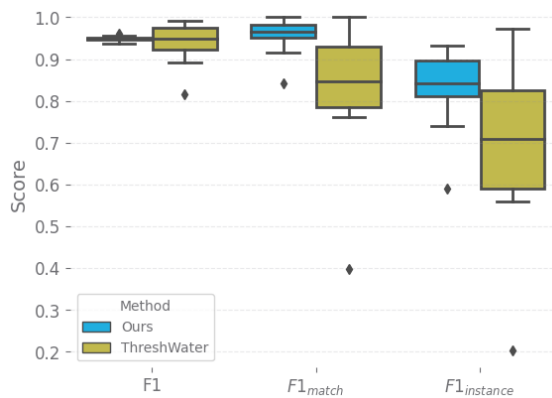


Figure 7: Segmentation quantification results of the in-distribution set for each sample. Higher is better.

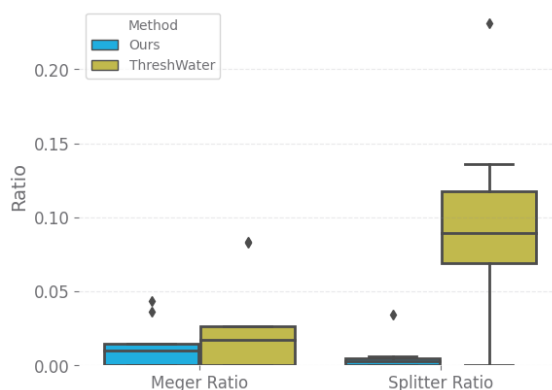


Figure 8: Separation quantification results of the in-distribution set for each sample. Lower is better.

Name	Merger Ratio	Num Mergers	Splitter Ratio	Num Splitters
ThreshWater	0.0267	88	0.0902	329
Ours	0.0131	64	0.0058	11

Table 3

The separation quantification results of the in-distribution set of our method compared to ThreshWater. Lower is better.

5.1.2. Out-Of-Distribution evaluation

In contrast to the in-distribution (ID) test set, the out-of-distribution (OOD) test set contains samples with minerals, particle sizes, and particle shapes that are not present in the training dataset. Thus, this evaluation provides valuable information on how well our method performs on samples with different characteristics not seen before and consequently highlights how it can be expected to generalize to a wider scope of use-cases. Our out-of-distribution test set contains 5 annotated patches from 5 different samples. The quantitative analysis is analogous to the previous section. The $F1$, the $F1_{match}$, and $F1_{instance}$ results of our method and ThreshWater are shown in Figure 9 and Table 4. On average our method reaches on the OOD set a $F1$ of 93.27%, a $F1_{match}$ of 89.18%, and a $F1_{instance}$ of 72.77%. The OOD $F1$ and thus the general foreground prediction quality has only a slight reduction of 1.57% when compared against our ID $F1$ score. The $F1_{match}$ score in contrast, has a reduction of 5.98% on the OOD set. This dropoff between OOD and ID is even more considerable for the $F1_{instance}$ with a reduction of 9.36%. The reduction for both metrics can be traced to the sample Ore4_PS_Tmp4, which includes a high number of very small particles (<??mm) that have only a diameter of 1-2 voxels and are of very low contrast. Thus even for humans, these particles are almost indistinguishable from the background, making them hardly detectable for our model. We highlight the challenges associated with this sample as part of our qualitative evaluation in section 5.2.6. When Ore4_PS_Tmp4 is excluded from the evaluation a $F1_{match}$ of 96.94% and an $F1_{instance}$ of 84.52% are achieved, which is on par with the results from the in-distribution set. An even more drastic reduction in $F1_{match}$ and $F1_{instance}$ can be observed with ThreshWater, achieving only 63.11% and 44.88%, respectively. However, in contrast to our method, ThreshWater consistently performs worse over almost all samples, indicating a failure to generalize. This demonstrates that our method is not only considerably better than ThreshWater but also that it is applicable in practice as it generalizes well to unknown materials and minerals, while producing segmentations of excellent quality when adhering to a minimum particle size of XXX mm.

We continue the out-of-distribution evaluation with the separation quality shown in Figure 10. This set consists of 1045 particles of which only 29 particles (2.55%) touch each other as a result of our sample preparation strategy. Of those 29 touching particles only 14 are not predicted as individual instances, which is only 0.97% of all particles. The baseline ThreshWater achieves minimally better results with only 10 Mergers as shown in Table 5. However, when taking the number of Splitters into account, our method only

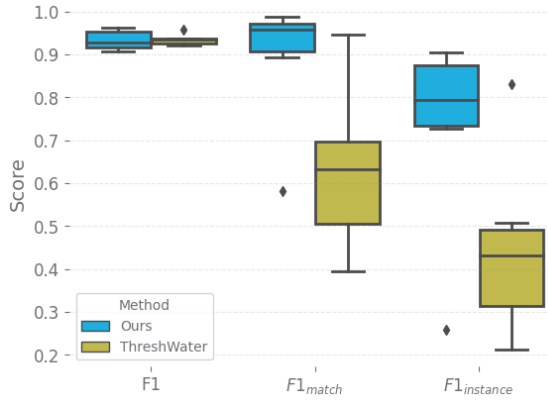


Figure 9: Segmentation quantification results of the out-of-distribution set for each sample. Higher is better.

Name	$F1$	$F1_{match}$	$F1_{instance}$
ThreshWater	0.9347	0.6311	0.4488
Ours	0.9327	0.8918	0.7277

Table 4

The segmentation quantification results of the out-of-distribution set of our method compared to ThreshWater. Higher is better.

Name	Merger Ratio	Num Mergers	Splitter Ratio	Num Splitters
ThreshWater	0.0091	10	0.554	188
Ours	0.0097	14	0.0048	2

Table 5

The separation quantification results of the out-of-distribution set of our method compared to ThreshWater. Lower is better.

produces 2 Splitters (0.48% in the mean), while ThreshWater produces 188 (55.4% in the mean). This demonstrates again the deficit of ThreshWater to reliably identify individual particles as instances, while our method performs well on this task and even achieves slightly better results than on the in-distribution set.

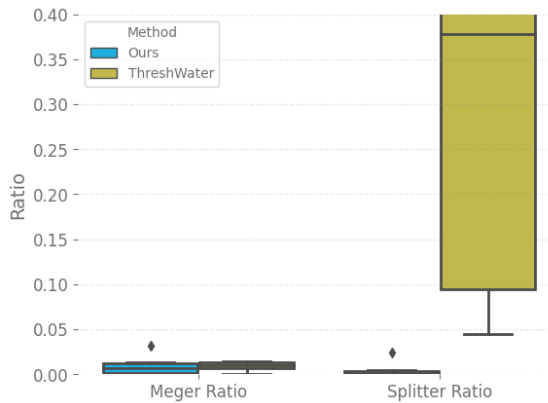


Figure 10: Separation quantification results of the out-of-distribution set for each sample. Lower is better.

5.2. Qualitative evaluation

We conducted a qualitative evaluation of the test samples and other collected samples. An overview of some samples and our inferred predictions is given in Figure 11. Besides a general sample overview, we also selected several particles and their prediction from these cases for further discussion. The prediction of each such particle can be categorized into one of six categories depending on the prediction quality and potential failure cases. These categories are discussed in the following subsections.

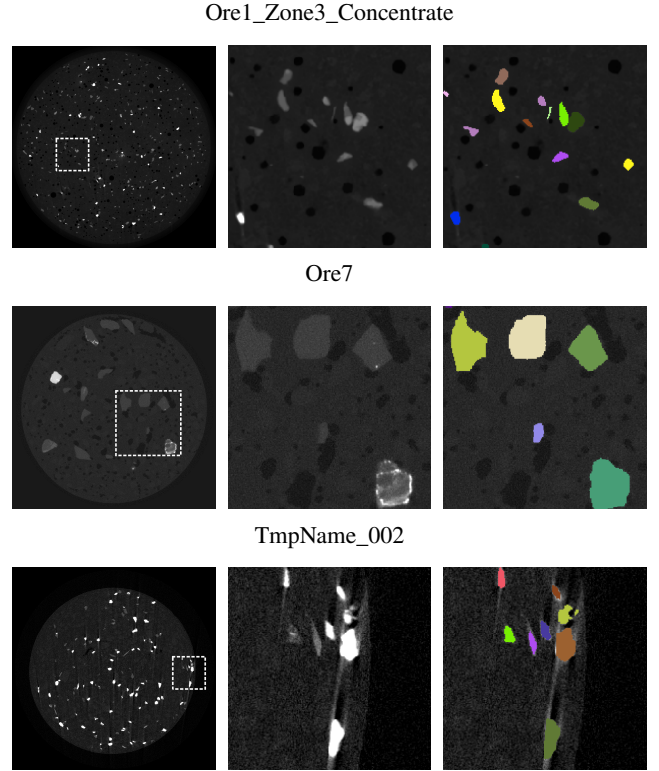


Figure 11: Overview of samples with different appearances, varying particle sizes, and CT imaging artifacts. Left: 2D view of the entire image; Middle: Zoomed crop of the image; Right: Prediction of our method for the crop

5.2.1. High quality

Most particles are generally predicted with high quality by our method and a random subset of them have been chosen for visualization. ThreshWater also predicts most of these particles in high quality (green), yet some particles are of lower contrast (orange), leading to less precise borders inferred by ThreshWater. Examples of the high-quality particles compared to ThreshWater are shown in Figure 12. These include particles from a variety of different materials and minerals with a large window of different intensities and appearances. It can be seen that our method performs well even on multi-phase particles.

5.2.2. Artifacts

CT artifacts such as beam-hardening or streak artifacts can greatly alter the particle appearance and affect even

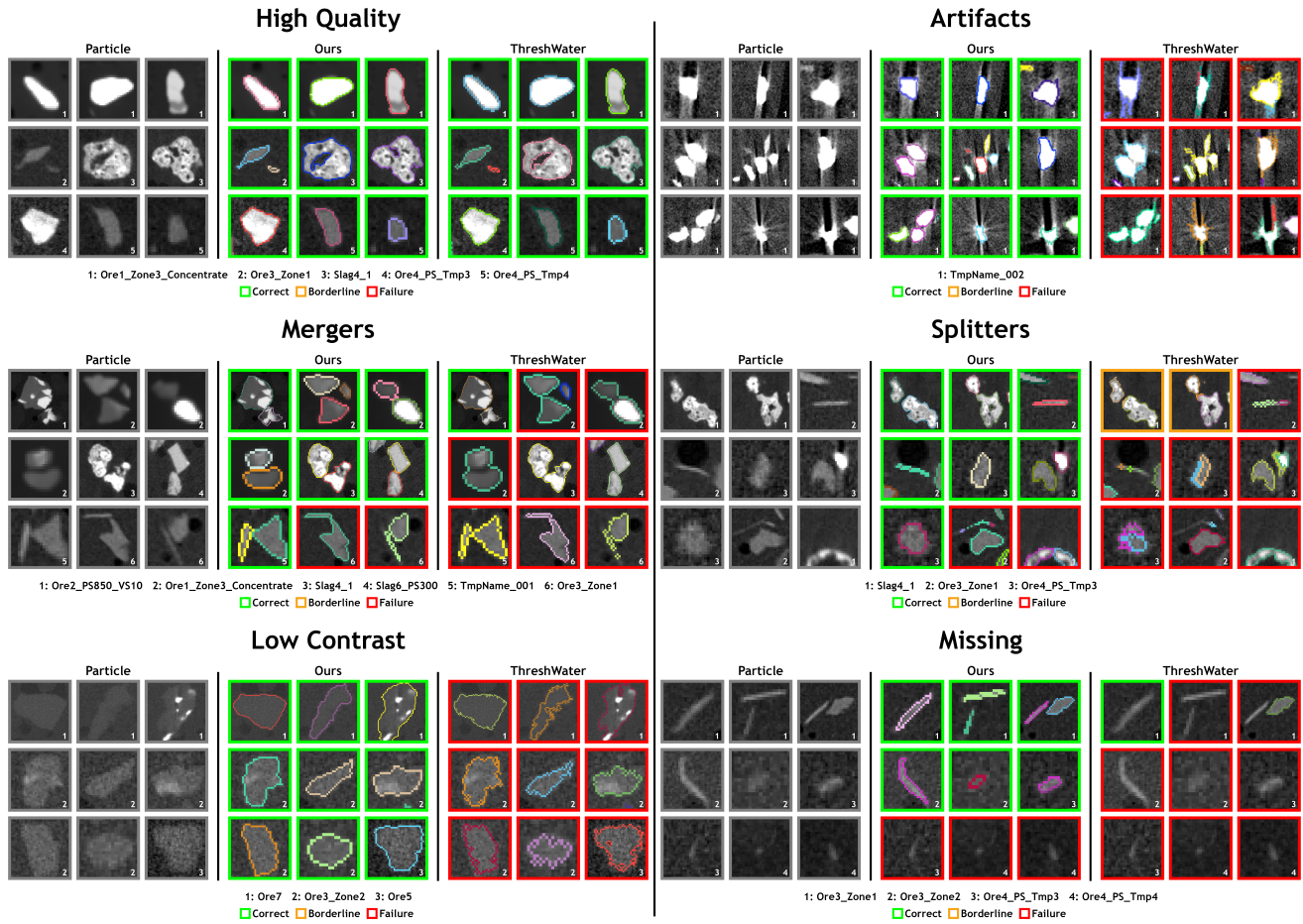


Figure 12: Qualitative comparison of high quality particles predicted by our method and by ThreshWater.

nearby particles. Examples of such artifacts are shown in Figure 12. These types of artifacts are especially challenging for classical segmentation approaches. As can be seen on the predicted particles by ThreshWater, entire streaks that are outgoing from particles are segmented, often merging nearby particles as a result. By contrast, our method delineates more realistic predictions of particle borders affected by such artifacts. Even when multiple particles affected by artifacts are clustered in close proximity, our method predicts well-defined particle borders. This again demonstrates the advantage of deep-learning methods that rely on learned image features in contrast to classical methods which mostly rely on image intensities.

5.2.3. Mergers

A Merger (see section 4.1) is a group of two or more touching particles incorrectly predicted as a single instance. Examples of such merged particles and correctly separated particles are shown in Figure 12. As can be seen, many touching particles are correctly separated by our method, yet for some, our method also fails. This is mostly the case when the two touching particles are too intertwined with each other so that our model is unable to recognize them as individual instances. However, there are also failure cases

with one of the two touching particles being too thin. This is due to our small core filter explained in section 3.2.2. As some particles have a diameter of only 1-3 voxels, our filter removes their core as it might be faulty. As a consequence, it is not possible to correctly identify these long thin particles as separate instances in case they touch another particle. In practice, this does not happen often and our method, therefore, produces only a very low number of Mergers as discussed in our quantitative evaluation in section 5.1. By contrast, ThreshWater produces noticeably more Mergers, especially in cases where our method correctly identifies them as separate instances.

5.2.4. Splitters

A Splitter (see section 4.1) is a particle incorrectly predicted as multiple particles. Examples of such Splitter particles but also of correctly identified particles are shown in Figure 12. Our method produces only a neglectable small number of Splitters. A direct cause for these few cases could not be identified. By contrast, ThreshWater produces a significantly higher number of Splitters, which originate mostly from noisy predictions on low-contrast samples. In turn, this can lead to disconnected regions within a particle resulting in a Splitter. When comparing these cases to the

results of our method, we see that our method is robust against these failure cases.

5.2.5. Low contrast

A noisy particle prediction is a prediction with inconsistent fuzzy borders. The cause for such a noisy prediction is usually a low contrast of particles to background in addition to high image noise. Examples of such noisy particle predictions are shown in Figures 12. It can be seen that the baseline ThreshWater is highly affected by this problem and predicts almost all particles with noisy particle masks in such low-contrast high-noise images. By contrast, our method is robust against such issues and consistently predicts the particle masks in high quality even under such difficult imaging conditions.

5.2.6. Missing

It is possible that the method used for inference completely fails to detect a particle, which results in no particle mask being predicted for the given particle. Examples of such missed particles are shown in Figure 12. For our method, this mostly happens in low-contrast high-noise images with particles having a diameter below 3 voxels. Therefore, it can be concluded that 4 voxels are the detection limit of our model. Smaller particles can be detected but the reliability is compromised. It is therefore proposed that this detection limit is used as a guideline for future work. By contrast, ThreshWater also fails on larger particles and thus has a worse detection limit. These particles tend to be long thin particles that have a minimum diameter of 3 voxels. In these cases, the particle mask is filtered away due to the noise reduction step. The noise reduction step is necessary for ThreshWater to perform well at all, but creates such missed particles in the process.

5.3. Inference time evaluation

We conduct an evaluation on the impact of different particle sizes and image sizes on the inference time and deduce advantages and limitations of our method. Both the in-distribution and out-of-distribution test sets are used for the analysis. Given some fixed hardware, here a Nvidia A100 GPU (Nvidia, Santa Clara, USA), the inference time only depends on the number of patches extracted and passed to nnU-Net for predicting (Section 3.3) a given image. This relationship is investigated in Figure 13. The number of patches, in turn, depends on the image size and the *ParticleSize* in voxels, with the latter being determined manually (see Section 3.2.1) and can be computed with Equation 7.

$$\text{ParticleSize voxel} = \frac{\text{ParticleSize mm}}{\text{Voxel Spacing mm}} \quad (7)$$

Figure 13 also shows the impact of the different particle sizes on the inference time, with different image sizes being represented as circles with varying diameters. On average, our dataset has a particle size of 60 ± 32 voxels and an image size of $(997 \pm 287, 1256 \pm 218, 1256 \pm 218)$ voxels. The inference time for one image is on average 12.09 ± 20.01 hours (median 4.41 hours). When inspecting Figure 5.3.D,

we see that with a particle size of 60 or larger the inference time takes less than 2 hours. However, with a particle size of 60 to 40, the inference time quickly increases to 10 hours. Particle sizes below 40 become increasingly computationally intensive with inference times of 30 or even 72 hours. This exponential rise in inference times originates from the particle size normalization (Section 3.2.1). While having a manageable impact down to a particle size of 50, our method becomes resource intensive the smaller the particles are. In this manuscript, the target particle size for the particle size normalization was meticulously chosen, along with a corresponding border thickness, to maximize performance on our diverse training dataset. In this setting, small target particle sizes could lead to excessive downsampling of large particles, causing a loss in border quality when resizing the predictions back to the original particle size. Conversely, large target particle sizes may cause excessive upscaling during inference and thus cause impractical prediction times. With the goal of using the model for a large number of samples, we focused on striking a good balance between segmentation quality and inference times. For narrower application windows, a specifically optimized target particle size along with a retraining of our model could be conceivable.

6. Conclusion

Mineral resources are finite and must be acquired cost-effectively and responsibly through advances in exploration, processing, and recycling. Hereby, the characterization of individual particles plays a crucial role in enabling and optimizing automation in the face of rising demand.

In the wake of increasingly sophisticated processing techniques, there is an ever-growing need for characterizing individual particles over bulk characterization. Throughput and the ability to quickly analyze new, unique samples are key to catalyze future progress.

One key step towards characterizing individual particles is to isolate them from 3D images containing up to tens of thousands of such particles through a process called instance segmentation. In this manuscript, we presented a new deep learning framework capable of just that. By leveraging the power of the nnU-Net framework, as well as the border-core representation to perform instance segmentation, our method is able to substantially outperform the currently used approaches in the field with respect to segmentation accuracy, its ability to separate touching particles as well as its robustness to varying particle sizes, imaging artifacts, and unseen mineral types. Our extensive evaluation on the out-of-distribution test set underlines how our method can be applied even to previously unseen minerals without requiring retraining. In the context of current practices in the field where new training data needs to be collected and the algorithm needs to be retrained for each image, our solution constitutes a substantial workflow improvement and unlocks previously impossible levels of scalability. For the vast majority of samples, it can simply be used to make predictions with no further human input required.

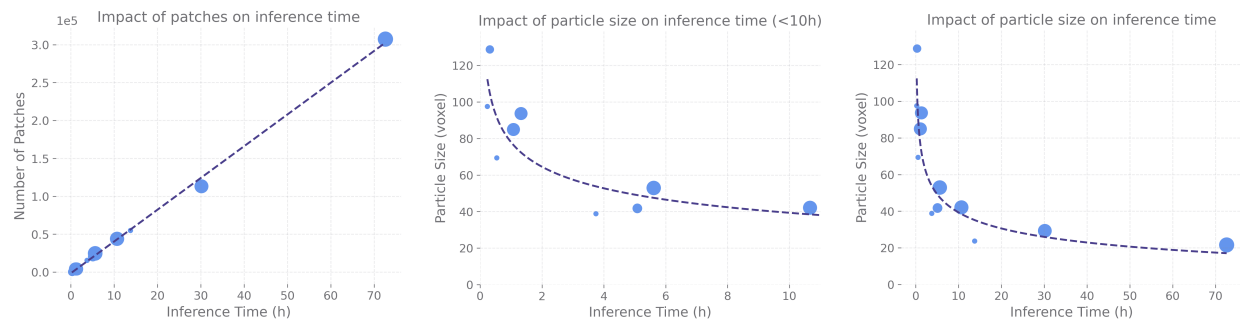


Figure 13: Impact of the number of patches used by nnU-Net for prediction and of the particle size on the inference time. Evaluated on in-distribution and out-of-distribution test sets with the marker size being proportional to the respective image size.

Our method is thus well positioned to greatly enhance scalability and precision of individual particle characterization in a standardized way and will thus act as a catalyst for accelerating the development of exploration, processing, and recycling strategies.

All code and datasets are made publicly available along with instructions on how to use them.

Acknowledgement

Part of this work was funded by Helmholtz Imaging (HI), a platform of the Helmholtz Incubator on Information and Data Science.

References

Baraian, A., Kellokumpu, V., Paaso, J., Koresaar, L., Kaartinen, J., 2022. Computing particle size distribution of mineral rocks using deep learning-based instance segmentation, in: 2022 10th European Workshop on Visual Information Processing (EUVIP), IEEE. pp. 1–6.

Becker, M., Jardine, M., Miller, J., Harris, M., 2016. X-ray computed tomography: A geometallurgical tool for 3d textural analysis of drill core. See AusIMM (2016) , 231–240.

Blannin, R., Frenzel, M., Tuşa, L., Birtel, S., Ivăşcanu, P., Baker, T., Gutzmer, J., 2021. Uncertainties in quantitative mineralogical studies using scanning electron microscope-based image analysis. Minerals Engineering 167, 106836.

Dominy, S., Platten, I., Howard, L., Elangovan, P., Armstrong, R., Minnitt, R., Abel, R., 2011. Characterisation of gold ores by x-ray computed tomography—part 2: Applications to the determination of gold particle size and distribution, in: Proceedings of the First AusIMM International Geometallurgy Conference, Brisbane, Australia, pp. 5–7.

Filippo, M.P., Gomes, O.d.F.M., da Costa, G.A.O.P., Mota, G.L.A., 2021. Deep learning semantic segmentation of opaque and non-opaque minerals from epoxy resin in reflected light microscopy images. Minerals Engineering 170, 107007.

Furat, O., Kirstein, T., Leißner, T., Bachmann, K., Gutzmer, J., Peuker, U.A., Schmidt, V., 2023. Multidimensional characterization of particle morphology and mineralogical composition using ct data and r-vine copulas. arXiv preprint arXiv:2301.07587 .

Godinho, J., Kern, M., Renno, A., Gutzmer, J., 2019. Volume quantification in interphase voxels of ore minerals using 3d imaging. Minerals Engineering 144, 106016.

Godinho, J.R., Grilo, B.L., Hellmuth, F., Siddique, A., 2021. Mounted single particle characterization for 3d mineralogical analysis—mspacman. Minerals 11, 947.

Guntoro, P.I., Ghorbani, Y., Parian, M., Butcher, A.R., Kuva, J., Rosenkranz, J., 2021. Development and experimental validation of a texture-based 3d liberation model. Minerals Engineering 164, 106828.

Hassan, N.A., Airey, G.D., Khan, R., Collop, A.C., 2012. Nondestructive characterisation of the effect of asphalt mixture compaction on aggregate orientation and segregation using x-ray computed tomography. International Journal of Pavement Research and Technology 5, 84.

Isensee, F., Jaeger, P.F., Kohl, S.A., Petersen, J., Maier-Hein, K.H., 2021. nnu-net: a self-configuring method for deep learning-based biomedical image segmentation. Nature methods 18, 203–211.

Jiang, S., Shen, L., Guillard, F., Einav, I., 2021. Characterisation of fracture evolution of a single cemented brittle grain using in-situ x-ray computed tomography. International Journal of Rock Mechanics and Mining Sciences 145, 104835.

Latif, G., Bouchard, K., Maitre, J., Back, A., Bédard, L.P., 2022. Deep-learning-based automatic mineral grain segmentation and recognition. Minerals 12, 455.

Liu, X., Zhang, Y., Jing, H., Wang, L., Zhao, S., 2020. Ore image segmentation method using u-net and res_unet convolutional networks. RSC advances 10, 9396–9406.

Liu, Y., Zhang, Z., Liu, X., Wang, L., Xia, X., 2021. Efficient image segmentation based on deep learning for mineral image classification. Advanced Powder Technology 32, 3885–3903.

Nie, X., Zhang, C., Cao, Q., 2022. Image segmentation method on quartz particle-size detection by deep learning networks. Minerals 12, 1479.

Pereira, L., Frenzel, M., Khodadadzadeh, M., Tolosana-Delgado, R., Gutzmer, J., 2021. A self-adaptive particle-tracking method for minerals processing. Journal of Cleaner Production 279, 123711.

Sofroniew, N., Lambert, T., Evans, K., Nunez-Iglesias, J., Bokota, G., Winston, P., Peña-Castellanos, G., Yamauchi, K., Bussonnier, M., Pop, D.D., et al., 2022. napari: a multi-dimensional image viewer for python. Zenodo .

Sun, G., Huang, D., Cheng, L., Jia, J., Xiong, C., Zhang, Y., 2022. Efficient and lightweight framework for real-time ore image segmentation based on deep learning. Minerals 12, 526.

Tang, K., Da Wang, Y., Niu, Y., Honeyands, T.A., O'Dea, D., Mostaghimi, P., Armstrong, R.T., Knackstedt, M., 2023. Particle classification of iron ore sinter green bed mixtures by 3d x-ray microcomputed tomography and machine learning. Powder Technology 415, 118151.

Tung, P.K.M., Halim, A.Y., Wang, H., Rich, A., Marjo, C., Regenauer-Lieb, K., 2022. Deep-xft: Deep learning 3d-mineral liberation analysis with micro-x-ray fluorescence and computed tomography. Energies 15, 5326.

Van der Walt, S., Schönberger, J.L., Nunez-Iglesias, J., Boulogne, F., Warner, J.D., Yager, N., Gouillart, E., Yu, T., 2014. scikit-image: image processing in python. PeerJ 2, e453.

Wang, W., Li, Q., Xiao, C., Zhang, D., Miao, L., Wang, L., 2021. An improved boundary-aware u-net for ore image semantic segmentation. Sensors 21, 2615.

Wang, Y., Lin, C., Miller, J., 2015. Improved 3d image segmentation for x-ray tomographic analysis of packed particle beds. Minerals Engineering 83, 185–191.

Wang, Y., Lin, C., Miller, J., 2016. 3d image segmentation for analysis of multisize particles in a packed particle bed. Powder Technology 301, 160–168.

Xiao, D., Liu, X., Le, B.T., Ji, Z., Sun, X., 2020. An ore image segmentation method based on rdu-net model. *Sensors* 20, 4979.

Zhou, X., Dai, N., Cheng, X., Thompson, A., Leach, R., 2021. Three-dimensional characterization of powder particles using x-ray computed tomography. *Additive Manufacturing* 40, 101913.